Reactive Power Minimization in Bidirectional DC–DC Converters Using a Unified-Phasor-Based Particle Swarm Optimization

Haochen Shi, Huiqing Wen, *Member, IEEE*, Yihua Hu, *Senior Member, IEEE*, and Lin Jiang, *Member, IEEE*

***Abstract*—This paper deals with an optimized three-level modulated phase shift control using particle swarm optimization (PSO) strategy based on the unified phasor analysis with an aim to improve the efficiency of the bidirectional dual active bridge (DAB) converter for the whole operation range. A unified mathematical model based on Fourier transform is built for the DAB converter. All possible operation states under the three-level modulated phase shift control are covered. Accurate complex mathematical expressions for the inductor current, the transmission power, and the reactive power are obtained. Both modulus and angle variables are illustrated with respect to the inner and outer phase shift angle with the phasor diagram. The proposed method is able to achieve the minimum reactive power under three-level modulated phase shift control by obtaining the optimal phase-shift angles directly. The cumbersome process of the optimal operation mode selection for different voltage conversion ratio and load conditions in conventional methods is overcome successfully, thus greatly simplifying the theoretical calculation and implementation difficulty. Simulation and experimental results in terms of the reactive power, soft-switching range, and efficiency are provided to verify the practical feasibility of the proposed method for the bidirectional DAB converters.**

***Index Terms*—Bidirectional dc–dc converter, particle swarm optimization (PSO), reactive power, three-level modulated phase shift control, unified phasor analysis.**

I. Introduction

As a key component of the high-frequency power transmission system, the isolated bidirectional dc–dc converter (IBDC) is essential to achieve a bidirectional power flow and

---

Manuscript received September 11, 2017; revised January 8, 2018; accepted February 20, 2018. Date of publication March 15, 2018; date of current version September 28, 2018. This work was supported by the National Nature Science Foundation of China (51407145), the Jiangsu Science and Technology Programme (BK20161252), the Suzhou Prospective Application Programme (SYG201723), and the Research development fund of XJTLU (RDF-16-01-10). Recommended for publication by Associate Editor Prof. H. Li. *(Corresponding author: Huiqing Wen.)*

H. Shi is with the Xi’an Jiaotong-Liverpool University, Suzhou 215123, China. (e-mail:

conduction loss and it is related to the rms current. The current stress can be regarded as a symbol of the rms current under the same output power, so the current-stress-optimized (CSO) control is proposed to minimize the peak current with the same rated power [26]–[28]. Moreover, the efficiency-optimized control schemes including conduction losses and switching losses are also presented in [29]–[31]. Those optimized control methods can dramatically decrease the losses and improve efficiency.

However, the mathematical model of the three-level modulated phase shift method needs to build as piecewise functions for different operation condition and time intervals [20]. The piecewise time domain expression is complicated and inconvenient in the analysis of the functioning status and the design of a control system. As the result, the CSO and efficiency-optimized control scheme in [26] and [29] need to be divided into separate optimized sections in terms of different load condition and voltage conversion ratio. The TPS has three control freedoms and it has to be divided into six operation modes according to different conditions among three phase-shift variables, which are illustrated in [11, Fig. 7]. Multiple operation modes make the mathematical expressions for relevant parameter such as transmission power, inductor rms current, and reactive power complicated since they are varying with different operation modes [22]. In order to search the global optimization algorithms of TPS control, all operation modes need to be considered, which significantly increases the complexity of optimization algorithms. Besides, the complexity of the piecewise time domain expression makes the algorithm implementation in a real microcontroller difficult. For instance, the optimal operation mode selection for different voltage conversion ratio and load conditions is necessary in conventional methods, which is a cumbersome process since there are in total 8 and 12 submodes in EPS and TPS control, respectively [20]. The target optimization functions for different modes under DPS, which are different power loss components of DAB converters, are listed in [29, Table IV]. The Lagrangian optimization method is used to obtain the optimal phase-shift pairs [29]. This process is complex since it requires multiple partial differential calculations. Furthermore, the optimal phase-shift angles must be calculated in an offline manner and then imported into the microcontroller [29]. To avoid the complexity of piecewise time domain expressions, a universal high-frequency-link (HFL) expression is proposed to unify all states of the TPS by a global mathematical model. Based on global HFL expression, the PWM plus phase-shift control is adopted in order to reduce the reactive current [32]. However, similar to the research in [18], the definition of the reactive current is incomplete since only the input-side reactive current is considered. Considering both input-side and output-side reactive current for all possible operation modes, the mathematical expressions are very complicated and the seeking for the optimal phase-shift angles is a time-consuming process.

Many advanced iterative techniques have been utilized for solving optimization problems such as the Lagrange multiplier method [25], Newton's method [33], mathematical programing methods [34], and genetic algorithm (GA) [35]. However, these techniques show obvious limitations such as heavy computational burden, high dependence on the initial guess setting, and detailed model knowledge. To address this issue, particle swarm optimization (PSO), a method inspired by insect swarm behavior for food search, can be easily applied for the control optimization problems such as the passive filter design [36], elimination of harmonics [37], and resonant controller parameters tuning [38]. In this paper, a PSO optimization method based on the unified phasor analysis in the frequency domain is proposed for the bidirectional DAB converter. Main control objective is to obtain the optimal phase-shift angles under three-level modulated phase shift control that achieves the minimum reactive power of the DAB converter. Compared with GA and other optimization methods, the proposed PSO needs less parameters to adjust, less computational burden, and faster convergence speed. Furthermore, the unified phasor model is built in the frequency domain according to the Fourier transformation, unified and accurate complex mathematic expressions for the transmission power and the reactive power are obtained for the optimization. Thus, the optimization removes the cumbersome process of the optimal operation mode selection for different voltage conversion ratio and load conditions in conventional methods, which simplifies the theoretical calculation and the practical implementation. Main analytical and experimental results are presented to demonstrate the validity and effectiveness of the proposed optimization method.

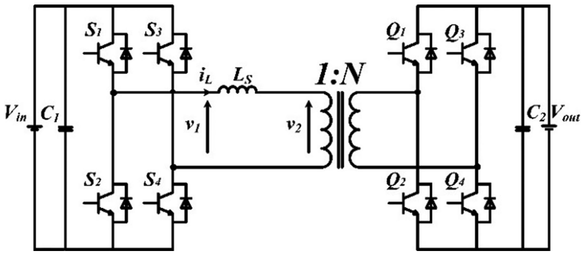

Fig. 1. DAB converter topology.

II. UNIFIED HARMONICS ANALYSIS UNDER THREE-LEVEL MODULATED PHASE SHIFT CONTROL

A. Three-Level Modulated Phase Shift Control

Fig. 1 shows the typical structure of the DAB converter, where the primary and secondary bridges are connected via high frequency (HF) transformer and auxiliary inductor L_s. For any two switches in the same bridge arm, their duty cycle signals are complementary. In Fig. 1, L_S is equivalent as sum of the auxiliary inductor and transformer leakage inductor, i_L is the inductor current, V_{in} and V_{out} are the input and output port dc voltage, v_1 is the three-level square-wave voltage of the primary side bridge and v_2 is the three-level square-wave voltage of the secondary side bridge refer to the primary side, and N is the turns ratio of the transformer.

The universal waveforms with a universal three-level modulated phase shift control are shown in Fig. 2. The angle θ_1 and θ_2 represent the inner phase shift angle for the three-level square wave v_1 and v_2. Specifically, the zero-level duration for the three-level voltage v_1 and v_2, respectively, which brings the benefit in reducing the reactive current by circulating the current

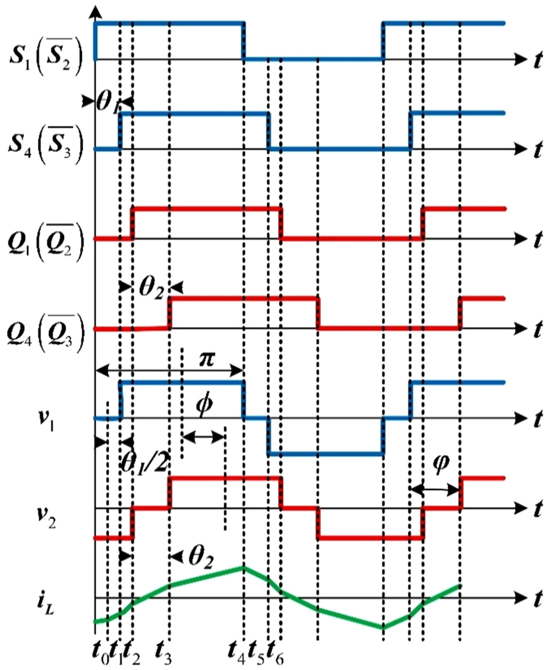

Fig. 2. Typical waveforms with the three-level modulated phase shift method.

inside each bridge instead of backing into the input or output side. The phase shift φ is the traditional phase shift or the outer phase shift, which is indicated in the phase shift between the rising edge of v_1 and v_2. For the convenience of the control, the outer phase shift φ is replaced by the center point outer phase shift Φ, which is defined as the phase difference between the center points of pulse width of v_1 and v_2. As indicated in Fig. 2, the relationship between the center point outer phase shift Φ and other phase shift angles is $\phi = \varphi + (\theta_1 - \theta_2)/2$. Thus, with this definition, a universal three-level modulated phase shift control gives three independent control variables, namely θ_1, θ_2, and Φ. The other control methods can be regarded as a special case. For example, SPS is a special case when $\theta_1 = \theta_2 = 0$, and tradition outer phase shift φ is equal to the center point phase shift Φ.

According to [37] and [38], the harmonic form of the asymmetric waveform of v_1 and v_2 will lead to complex expression for the inductor current, which will increase the difficulty of the analysis about the active and reactive power as well as the soft-switching region. So t_0 for the three-level square wave is set at $t_0 = \theta_1/2$, which allows the voltage v_1 symmetric and simplify the unified expression under the harmonic series form.

B. Unified Phasor Analysis of Inductor Current and Apparent Power

According to the Fourier series, the three-level square wave can be divided into a combination of the series odd order harmonics components. The ac link primary and secondary side voltage v_1 and v_2 can be rewritten as

$$\begin{cases} v_1(t) = \sum_{n=1,3,5,\ldots} \frac{4V_1}{n\pi}\cos\left(n\frac{\theta_1}{2}\right)\sin(n\omega_0 t) \\ v_2(t) = \sum_{n=1,3,5,\ldots} \frac{4V_2}{n\pi}\cos\left(n\frac{\theta_2}{2}\right)\sin(n\omega_0 t - \Phi) \end{cases} \tag{1}$$

where $\omega_0 = 2\pi f_s$ and f_s are the switching frequencies.

In (1), the primary and secondary voltage are described as the sum of the odd order sinusoidal components in the time-domain form. As illustrated in Fig. 1, for the same order component, v_1 is leading v_2 an outer phase shift Φ. Besides, the amplitude values for all order components of v_1 and v_2 are dependent on their inner phase shift angle θ_1 and θ_2, respectively. Since voltage v_1 and v_2 are periodic functions, they can be transferred into the phasor expressions in the complex number form as

$$\begin{cases} \dot{V}_1 = \sum_{n=1,3,5,\ldots} \frac{4V_1}{n\pi}\cos\left(n\frac{\theta_1}{2}\right) \\ \dot{V}_2 = \sum_{n=1,2,3,\ldots} \frac{4V_2}{n\pi}\cos\left(n\frac{\theta_2}{2}\right)\left[\cos(n\Phi) - j\sin(n\Phi)\right]. \end{cases} \tag{2}$$

Fig. 3 shows the phasor diagrams for $\dot{V}_1$, $\dot{V}_2$, $\dot{V}_L$, and $\dot{I}_L$, where $\dot{V}_1$ is the reference vector and it is always laid on the positive real axis. The phase of $\dot{V}_1$ is maintained at zero and the norm is $|\dot{V}_1| = (4V_1/n\pi)\cos(n\theta_1/2)$, which is decided by the input voltage amplitude V_1 and primary inner phase shift angle θ_1. The vector $\dot{V}_2$ is the secondary ac voltage, the norm of it is decided by the output voltage amplitude V_2, and secondary inner phase shift angle θ_2, which is $|\dot{V}_2| = (4V_2/n\pi)\cos(n\theta_2/2)$. According to (1) and (2), $\dot{V}_2$ is lagging angle Φ from $\dot{V}_1$. As illustrated in Fig. 1, $\dot{V}_1$ and $\dot{V}_2$ can be seen as connected via an ideal inductive reactance network. Thus, the inductor voltage can be seen as the difference between $\dot{V}_1$ and $\dot{V}_2$. The inductor voltage $\dot{V}_L$ can be calculated by the vector operation as

$$\dot{V}_L = \dot{V}_1 - \dot{V}_2 = \sum_{n=1,3,5,\ldots}\left[\frac{4V_1}{n\pi}\cos\left(n\frac{\theta_1}{2}\right)\right.$$
$$\left. - \frac{4V_2}{n\pi}\cos\left(n\frac{\theta_2}{2}\right)\left(\cos(\Phi) - j\sin(\Phi)\right)\right]. \tag{3}$$

Then, the reactance for the inductor is $Z_L = jn\omega L$, so the inductor current $\dot{I}_L$ can be calculated as

$$\dot{I}_L = \frac{\dot{V}_L}{Z_L} = \sum_{n=1,3,5,\ldots}\frac{4}{n^2\pi\omega_0 L}\left[V_2\cos\left(n\frac{\theta_2}{2}\right)\sin(n\Phi)\right.$$
$$\left. + j\left(V_2\cos\left(n\frac{\theta_2}{2}\right)\cos(n\Phi) - V_1\cos\left(n\frac{\theta_1}{2}\right)\right)\right]. \tag{4}$$

In Fig. 3, the relationship among $\dot{V}_1$, $\dot{V}_2$, $\dot{V}_L$, and $\dot{I}_L$, varied with outer phase shift angle Φ, is also illustrated. Re and Im represent the real and imaginary axis. The blue vector $\dot{V}_1$ is the reference vector and the vector length of it is equal to $|\dot{V}_1|$. The red vector $\dot{V}_2$ is lagging outer phase shift angle Φ from $\dot{V}_1$ and its length is equal to $|\dot{V}_2|$. Due to the outer phase shift $\Phi \in [-\pi, \pi]$, a complete phasor diagram for the DAB ac stage can be divided into four modes. The boundary of the $\dot{V}_2$ is the red half circle locus. The inductor voltage $\dot{V}_L$ is the black vector which is plotting from the tail of $\dot{V}_1$ to the tail of the $\dot{V}_2$. The inductor current $\dot{I}_L$ is lagging $\pi/2$ from the $\dot{V}_L$, which is plotted by the green line.

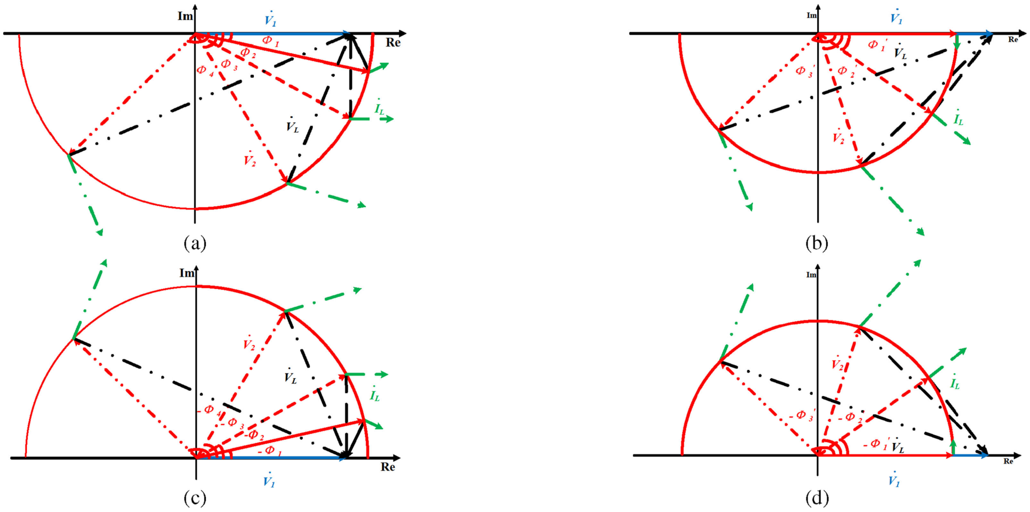

(a) (b)

(c) (d)

Fig. 3. (a) Phasor diagram for the DAB when $\dot{V}_1$ is leading $\dot{V}_2$ and $|\dot{V}_1| < |\dot{V}_2|$. (b) Phasor diagram for the DAB when $\dot{V}_1$ is leading $\dot{V}_2$ and $|\dot{V}_1| > |\dot{V}_2|$. (c) Phasor diagram for the DAB when $\dot{V}_1$ is lagging $\dot{V}_2$ and $|\dot{V}_1| < |\dot{V}_2|$. (d) Phasor diagram for the DAB when $\dot{V}_1$ is lagging $\dot{V}_2$ and $|\dot{V}_1| > |\dot{V}_2|$.

There are four operation states in Fig. 3(a) when the norm $|\dot{V}_1| < |\dot{V}_2|$. In the outer phase shift Φ_1 condition, the inductor current $\dot{I}_L$ is located in the first quartile, so both the active part and reactive current is positive. In the moment Φ_2, vector $\dot{V}_L$ is perpendicular to the vector $\dot{V}_1$, so $\dot{I}_L$ is parallel to the $\dot{V}_1$,which eliminates the reactive power. In that condition, $\dot{V}_1$, $\dot{V}_2$, and $\dot{I}_L$ consist of a right triangle, where

$$V_2 \cos\left(\frac{\theta_2}{2}\right) \cos(\Phi) = V_1 \cos\left(\frac{\theta_1}{2}\right). \tag{5}$$

The operation state for the Φ_1 and Φ_2 is similar. The phasor $\dot{I}_L$ is moving to the third quadrant, so the active current is still positive, while the reactive current becomes negative. Compared with the Φ_1 condition, the Φ_2 in the region $\Phi \in [\pi/2, \pi]$ clearly has higher reactive current with same active current due to the higher angle down from the real axis. The phasor diagram for the $|\dot{V}_1| > |\dot{V}_2|$ condition in Fig. 3(b) has similar variation condition, except it does not contain a positive reactive current condition like Φ_1 or the zero reactive current condition in Φ_2.

In the two-port network, the current flow in the network consists of the input and output current. In this single inductor network, the network current or inductor current, in this case, is the sum of the input and output current as follows:

$$\dot{I}_L = \dot{I}_{\text{in}} + \dot{I}_{\text{out}} = 2\dot{I}_{\text{in}}. \tag{6}$$

According to (2)–(6), the apparent power of the DAB can be calculated by the inductor current and primary side voltage with phasor analysis in the complex number form. Because the system is a two-port network, the apparent power includes both the input and output power. Besides, the reactive power can be generated by the same order components or mismatch order components [32]. In order to simply equations, the actual apparent power $\dot{S}_t = P_t + jQ_t$ can be normalized with a unified power $P_N = V_1{}^*V_2/(8f_s{}^*L)$, and the normalized apparent power $\dot{S}$, active power P, and reactive power Q can be obtained. Based on (1)–(6), the normalized apparent power $\dot{S}$ can be calculated as (7) shown at the bottom of this page, where P is the overall unified active power, Q is the overall unified reactive power, $Q_{m\,=\,n}$ is the unified reactive power caused by same order current and voltage components, $Q_{m\neq n}$ is the unified reactive power caused by different order current and voltage components, and $K = V_1/V_2$ is the voltage conversion ratio.

According to (7), the apparent power $\dot{S}$ is expressed by a sum of an infinite series. So the total amplitude of the apparent power $\dot{S}$ is related to the number of the harmonics components. Fig. 4 shows the unified reactive power Q varied with unified active power P with sum of different harmonics components. Curves for $m, n = 1$ and $m, n = 1, 3$ indicates that the increasing number of the harmonics components has obvious influences on the accuracy of the harmonics analysis. Furthermore, it can be seen that the impact of the number of harmonics components is de-

$$\begin{aligned}\dot{S} = \dot{V}_1 \dot{I}_{\text{in}} &= P + jQ = P + jQ_{m\,=\,n} + jQ_{mi\neq n} = \sum_{n=1,3,5,..} \frac{32}{n^3\pi^3}\left[\cos\left(n\frac{\theta_1}{2}\right)\cos\left(n\frac{\theta_2}{2}\right)\sin(n\Phi)\right]\\ &+ j\left[\sum_{n=1,3,5,..} \frac{32}{n^3\pi^3}\left[\cos\left(n\frac{\theta_1}{2}\right)\left[\cos\left(n\frac{\theta_2}{2}\right)\cos(n\Phi) - k\cos\left(n\frac{\theta_1}{2}\right)\right]\right]\right]\\ &+ j\left[\sum_{m,n=1,3,5,..} \frac{32}{mn^2\pi^3}\left[\cos\left(m\frac{\theta_1}{2}\right)\sqrt{\cos^2\left(n\frac{\theta_2}{2}\right) - 2k\cos\left(n\frac{\theta_1}{2}\right)\cos\left(n\frac{\theta_2}{2}\right)\cos(n\Phi) + k^2\cos^2\left(n\frac{\theta_1}{2}\right)}\right]\right]\end{aligned} \tag{7}$$

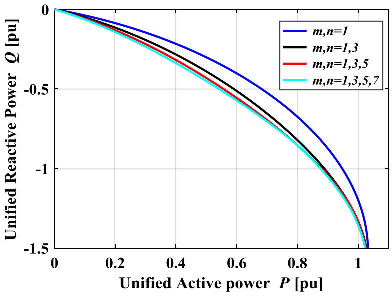

Fig. 4. Unified reactive power Q varied with unified active power P for different harmonics terms.

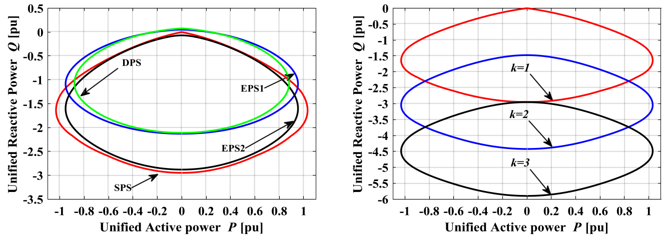

(a) (b)

Fig. 5. (a) Phasor diagram of unified reactive power Q varied with unified active power P using different control methods when $k = 1$. (b) Phasor diagram of unified reactive power Q varied with unified active power P under different voltage conversion ratio.

creasing with the increasing sum terms. For $m, n = 1, 3, 5$ and $m, n = 1, 3, 5, 7$, the difference is small and can be ignored. It is due to the coefficient of each component that is equal to $32/n^3\pi^3$, so the coefficient is inversely proportional to three times the power of n. Based on the above analysis, the number of harmonics components is limited to $m, n = 1, 3, 5, 7$ because the higher order has little impact on the analysis.

The apparent power $\dot{S}$ using different control methods with complex coordinate system is shown in Fig. 5. The X-axis is the real part or active power, whereas the Y-axis is the imaginary part or reactive power. Here, typical control strategies with specified phase-shift variables are illustrated and compared with the unified phasor method. Specifically, EPS1 is for the $\theta_1 = \pi/4, \quad \theta_2 = 0$, EPS2 is for $\theta_1 = 0, \quad \theta_2 = \pi/4$, DPS is for $\theta_1 = \pi/4, \quad \theta_2 = \pi/4$, and SPS is for $\theta_1 = 0, \quad \theta_2 = 0$. Compared with the traditional piecewise time-domain model, the apparent power $\dot{S}$ shows a closed locus under harmonics analysis. In the complex coordinate system, the positive or negative stand for the power transmission direction, and the amplitude is determined by absolute value. Specifically, the positive active power means the overall active power is transferring from v_1 to v_2, while the negative active power means the overall active power is transferring from v_1 to v_2. Due to the symmetry of the apparent power $\dot{S}$, there are two unequal reactive power to specify active power, which is caused by the symmetric function of the outer phase shift Φ_1 and Φ_2 in Fig. 3. In the practical design, the control with lower reactive power is usually used. The comparison among EPS, DPS, and SPS is illustrated in Fig. 5(a), which indicates that EPS and DPS can significantly reduce reactive power for the same transmission power compared with the SPS control. Furthermore, under the specified phase-shift conditions, EPS1 can reduce more reactive power than EPS2, while DPS shows similar reactive power reduction with EPS1.

Fig. 5(b) shows the phasor diagram of unified reactive power Q varied with unified active power P under different voltage conversion ratio k. For the condition of $k = 1$, the absolute value of reactive power is first increasing from zero with the increasing of the unified active power, then it is increasing with decreasing of the unified active power. The changing relationship between active and reactive power is similar for other values of k, the locus of the apparent power is translational and moving forward to the reactive axis. Fig. 5 shows that the unified phasor diagram can unify all possible strategies effectively for the DAB converter with bidirectional power flow capability. Since the relationship between active and reactive power for different controls can be accurately described by apparent power $\dot{S}$, a universal optimization method for bidirectional power flow condition can be obtained through the unified apparent power $\dot{S}$ according to the (7).

III. OPTIMIZED THREE-LEVEL MODULATED PHASE SHIFT CONTROL BY PSO

A. *Particle Swarm Optimization*

From the above analysis, the fundamental component is the taking majority value of active and reactive power in the DAB converter. So it can be used to represent actual active and reactive power with a negligible error. In order to improve the efficiency of the DAB converter, the minimum reactive power operation state with required active power must be located. It can be seen as a mathematical optimization problem that is aimed at finding the global extremum of the function subject to equality constraints. Considering the merits of PSO in terms of computational burden, parameter dependence, and convergence speed, here a PSO-based method is discussed under the aforementioned unified phasor expression.

In the PSO, a group of particles is moved by the equations which are related to their current position and velocity. The current position of particles is $X_i = (X_{i1}, \ldots, X_{\mathrm{id}})$, and the current velocity of particles is $V_i = (V_{i1}, \ldots, V_{\mathrm{id}})$. In order to determine the best behavior of particles, the objective function $f(x)$ is introduced to judge the behavior of the swarm. After choosing the objective function and constraints of the PSO calculation, the search procedure based on the historical position and velocity of each particle and their neighbors can be expressed as follows:

$$\begin{aligned} V_i(t+1) = \omega V_i(t) &+ c_1 \cdot \mathrm{rand} \cdot (P\mathrm{best}_i - X_i(t)) \\ &+ c_2 \cdot \mathrm{rand} \cdot (G\mathrm{best}_i - X_i(t)) \end{aligned} \quad (8)$$

where t is the iteration number, *rand* is a random number between 0 and 1, $P\mathrm{best}_i$ is the best position of ith particles, $G\mathrm{best}_i$ is the best position of all particles, c_1 and c_2 are the weighting factors, ω is the iteration weights factor, and d is the dimension of function.

The position of the particle is updated by the following:

$$\begin{aligned} X_i(t+1) &= X_i(t) + V_i(t+1) \\ X_i(t) &= (X_{i1}(t), \ldots, X_{\mathrm{id}}(t)). \end{aligned} \tag{9}$$

The update position of the swarm is determined by the historical position and updated velocity with the expressions as

$$\begin{aligned} P\mathrm{best}_i(t) &= (P\mathrm{best}_{i1}(t), \ldots, P\mathrm{best}_{\mathrm{id}}(t)) \\ G\mathrm{best}_i(t) &= (G\mathrm{best}_{i1}(t), \ldots, G\mathrm{best}_{\mathrm{id}}(t)). \end{aligned} \tag{10}$$

Expression (12) shows the best position for individual particle and an entire swarm of particles. If the current position of the individual particle is better than their historical position, $P\mathrm{best}_i$ will be updated as the current position. Furthermore, $G\mathrm{best}_i$ will be updated when swarm achieves a better position than historical swarm position.

The iteration weight factor can determine the influence of the previous particle velocity on the next particle velocity. The large iteration weight can enhance the global search ability at the starting iteration stage, while the small iteration weight can improve the speed of the global search. Here, a time-varying iteration weight factor is proposed for gaining selfadaption iteration weight factor, which can be calculated as follows:

$$\omega = \omega_{\max} - \frac{t}{t_{\max}} (\omega_{\max} - \omega_{\min}) \tag{11}$$

where $\omega_{\max}$ and $\omega_{\min}$ is the maximum and minimum value of the weight factor, *t* is the number of the inertia, and $t_{\max}$ is the maximum number of the inertia. In this paper, the upper limit $\omega_{\max} = 0.8$ and lower limit $\omega_{\min} = 0.2$. The weighting factor c_1 is also called the individuality weight which can determine the learning ability of the best historical position for the individual particle. The weighting factor c_2 is the global weight of the best historical position for global particle. In order to balance the individual and global learning ability, c_1 and c_2 are equal to 2 in this algorithm.

B. Objective Function for Minimizing the Reactive Power

In order to find the minimum reactive power operation point by the PSO, the objective function $f(x)$ is expressed as follows:

$$f(x) = \min\,[Q] \tag{12}$$

where *Q* is the overall reactive power with $m,\ n = 1, 3, 5, 7$.

According to (7), the objective function can be rewritten as (13) shown at the bottom of this page. In the same time, constraints based on the operation principle of the DAB converter are shown as follows:

$$\begin{cases} P = P_0 \\ \theta_1 \in [-\pi, \pi] \\ \theta_2 \in [-\pi, \pi] \\ \phi \in [-\pi, \pi] \end{cases} \tag{14}$$

where P_0 is desired active power. Those constraints can be divided into two categories, the linear constraint and the nonlinear constraint. The linear constraint $\theta_1 \in [-\pi, \pi], \theta_2 \in [-\pi, \pi], \phi \in [-\pi, \pi]$ is the upper and lower limit of three independent variables. It can easily be applied to the PSO algorithm by setting the upper boundary and lower boundary of variables $\theta_1, \theta_2,$ and ϕ. However, the nonlinear equality constraints $P = P_0$ are hard to directionally use in the PSO algorithm. So the penalty function can be used to achieve the constraint by adding penalty function into the objective function. It assumes that an objective function $F(\theta_1, \theta_2, \phi)$ consists of fitness function and penalty function which can be written as follows:

$$F(\theta_1, \theta_2, \phi) = Q(\theta_1, \theta_2, \phi) + \mu\alpha(\theta_1, \theta_2, \phi) \tag{15}$$

where $Q(\theta_1, \theta_2, \phi)$ is the fitness function of the reactive power, $\alpha(\theta_1, \theta_2, \phi)$ is the penalty function, and μ is the penalty coefficient. Since both the positive and negative reactive power components are considered, the absolute value of the fitness function $Q(\theta_1, \theta_2, \phi)$ will be used.

$$F(\theta_1, \theta_2, \phi) = |Q(\theta_1, \theta_2, \phi)| + \mu\alpha(\theta_1, \theta_2, \phi) \tag{16}$$

where the penalty function $\alpha(\theta_1, \theta_2, \phi)$ is used to address the unconstrained optimization problem. The penalty term on objective function can penalize any values which are greater than zero, which ensure that the minimum value of the penalty function is achieved when equality constraint is ensured. In this case, the nonlinear equality constraint $P = P_0$ is expressed as

$$P - P_0 = \cos(\theta_1/2)\cos(\theta_2/2)\sin(\phi) - P_0. \tag{17}$$

In order to ensure that the penalty term can add value when the constraint is violated, the equality constraint can be converted into a quadratic loss function that is expressed as

$$\alpha(\theta_1, \theta_2, \phi) = (P - P_0)^2 = (\cos(\theta_1/2)\cos(\theta_2/2)\sin(\phi) - P_0)^2. \tag{18}$$

According to penalty function (18), the minimum value of $\alpha(\theta_1, \theta_2, \phi)$ occurs when $P = P_0$. So the equality constraint is achieved in the objective function. Based on (16) and (18), the new unconstrained function $F(\theta_1, \theta_2, \phi)$ is adopted as (19)

$$\begin{aligned} Q(\theta_1, \theta_2, \phi) = &\sum_{n=1,3,5,..} \frac{32}{n^3\pi^3} \left[\cos\left(n\frac{\theta_1}{2}\right)\left[\cos\left(n\frac{\theta_2}{2}\right)\cos(n\Phi) - k\cos\left(n\frac{\theta_1}{2}\right)\right]\right] \\ &+ \sum_{m,n=1,3,5,..} \frac{32}{mn^2\pi^3}\left[\cos\left(m\frac{\theta_1}{2}\right)\sqrt{\cos^2\left(n\frac{\theta_2}{2}\right) - 2k\cos\left(n\frac{\theta_1}{2}\right)\cos\left(n\frac{\theta_2}{2}\right)\cos(n\Phi) + k^2\cos^2\left(n\frac{\theta_1}{2}\right)}\right] \end{aligned} \tag{13}$$

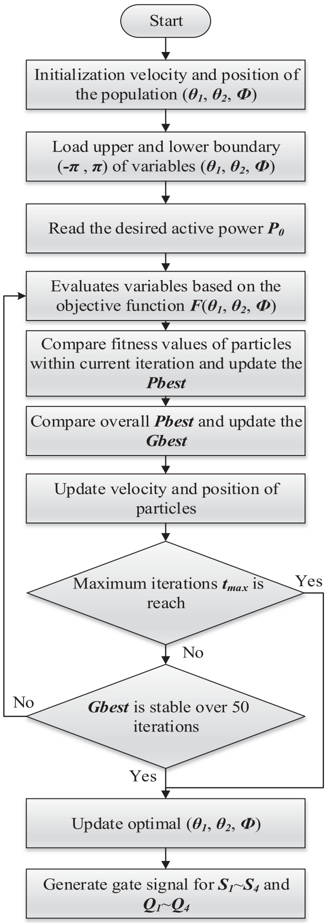

Fig. 6. Flowchart of the proposed PSO optimization method.

shown at the bottom of the page. In order to enhance the penalty function, the penalty coefficient μ is equal to 100. The objective function $F(\theta_1, \theta_2, \phi)$ can be used as the fitness function of the PSO control. The optimization flowchart is illustrated in Fig. 6. In the start stage, constraints for the fitness function includes lower and upper boundary and the desired active power P_0 for penalty function are loaded into the fitness 0 function. After that, the PSO algorithm will conduct fitness evaluation, then update *Pbest* and *Gbest* as well as the velocity and position of particles. The termination condition for the PSO algorithm is based on two criteria. If the maximum iteration $t_{\max}$ is reached or *Gbest* is stable over 50 generations. The stable criteria for *Gbest* is that the change of *Gbest* is less than 10^{-6} over 50 iterations. In this case, the minimum reactive power is already achieved so PSO needs to be force interrupted to reduce run time. After that, optimal variables $(\theta_1, \theta_2, \phi)$ are updated and gate signals are generated.

C. Comparative Evaluation of the Apparent Power by a Unified Phasor Diagram

Here, the proposed PSO-optimized phase-shift control (POPS) with the aim of the minimum reactive power is evaluated through MATLAB simulation. According to the principle of the PSO algorithm, the optimized position of the swarm continually updates the *Pbest* and *Gbest*, so the iteration number of generations may influence the final optimized position. The relationship between *Pbest* and *Gbest* varied with the maximum iteration $t_{\max}$ is shown in Fig. 7 when the voltage ratio $k = 2$ and desired unified transmission power $P_0 = 0.5$. It can be seen that the *Gbest* will be stabilized and the *Pbest* will approach the *Gbest* during the increase in the generations. According to Fig. 7(c), the *Pbest* has been reached and stabilized at the same level of the *Gbest* when $t_{\max} = 150$. It indicates that the optimization processing of the PSO algorithm needs enough number of iterations *t* to ensure the final optimized result, but the larger iteration will significantly raise the run time of the PSO optimization. Finally, the maximum iteration $t_{\max}$ is finally set as 300.

Fig. 8 shows the phase shift and reactive power varied with the number of iteration. It can be seen that phase shift with various unified active power condition requires different iteration number for stable. According to Fig. 8(a)–(c), the minimum stable generation number for $P = 0.2$, 0.4, 0.6, 0.8 is around $t = 55$, 40, 25, 10, so lower active power *P* needs larger stabilizing generation times. In Fig. 8(d), the increasing iteration number can significantly reduce the target reactive power until it reaches the global minimum reactive power. A smaller normalized active power condition *P* leads to larger initial reactive power and number of iteration for reaching minimum reactive power.

According to the above analysis, the apparent power of various control schemes including SPS, EPS, DPS, and POPS can be illustrated by the unified phasor analysis. Fig. 9(a) shows the locus of normalized reactive power varied with unified active power under different control methods. Specifically, parameters for these strategies are: EPS1 is with "$\theta_1 = \pi/4, \theta_2 = 0$," EPS2 is with "$\theta_1 = 0,\ \ \theta_2 = \pi/4$," DPS is with "$\theta_1 = \pi/4,\ \ \theta_2 = \pi/4$," and SPS is with "$\theta_1 = 0,\ \ \theta_2 = 0$." The outer phase shift

$$
\begin{aligned}
F(\theta_1, \theta_2, \phi) &= |Q(\theta_1, \theta_2, \phi)| + \mu\alpha(\theta_1, \theta_2, \phi) = \left| \sum_{n=1,3,5,..} \frac{32}{n^3\pi^3} \left[\cos\left(n\frac{\theta_1}{2}\right) \left[\cos\left(n\frac{\theta_2}{2}\right) \cos(n\Phi) - k \cos\left(n\frac{\theta_1}{2}\right) \right] \right] \right| \\
&\quad + \left| \sum_{m,n=1,3,5,..} \frac{32}{mn^2\pi^3} \left[\cos\left(m\frac{\theta_1}{2}\right) \sqrt{\cos^2\left(n\frac{\theta_2}{2}\right) - 2k\cos\left(n\frac{\theta_1}{2}\right)\cos\left(n\frac{\theta_2}{2}\right)\cos(n\Phi) + k^2\cos^2\left(n\frac{\theta_1}{2}\right)} \right] \right| \\
&\quad + \sum_{n=1,3,5,..} \mu \left[\frac{32}{n^3\pi^3} \cos\left(n\frac{\theta_1}{2}\right) \cos\left(n\frac{\theta_2}{2}\right) \sin(n\phi) - P_0 \right]^2 \qquad (19)
\end{aligned}
$$

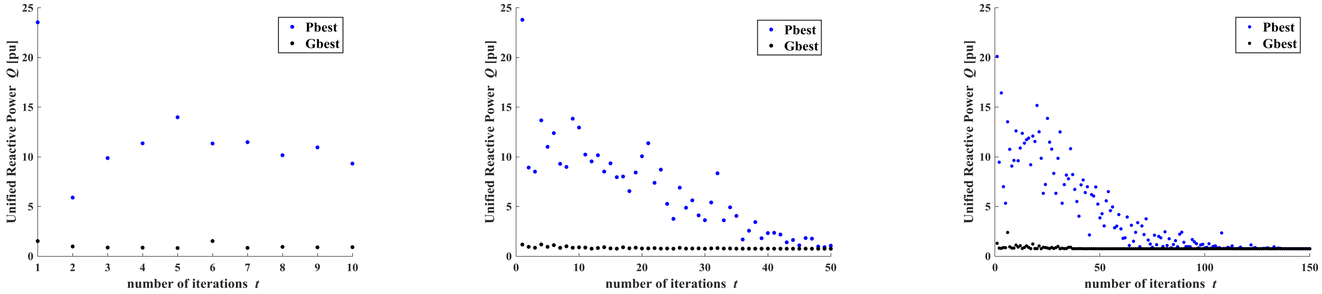

(a) (b) (c)

Fig. 7. (a) *Pbest* and *Gbest* of the unified reactive power Q varied with number of iteration when $t_{\max} = 10$. (b) *Pbest* and *Gbest* of the unified reactive power Q varied with number of iteration when $t_{\max} = 50$. (c) *Pbest* and *Gbest* of the unified reactive power Q varied with number of iteration when $t_{\max} = 150$.

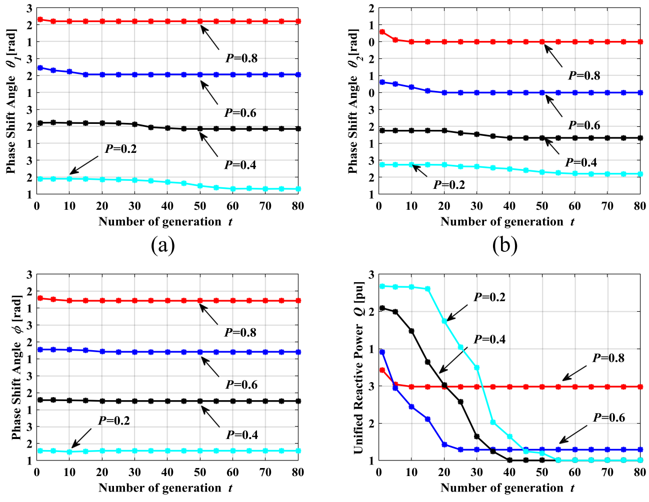

(a) (b) (c) (d)

Fig. 8. (a) Phase shift θ_1 varied with the number of iteration. (b) Phase shift θ_2 varied with the number of iteration. (c) Phase shift Φ varied with the number of iteration. (d) Reactive power Q varied with the number of iteration.

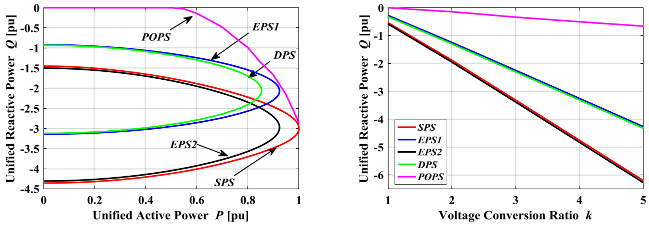

(a) (b)

Fig. 9. (a) Phasor diagrams of the positive direction apparent power for different control methods when $k = 2$. (b) Reactive power of different control methods when $P = 0.6$ varied with voltage conversion ratio k.

Φ belongs to $(0, \pi)$, the apparent power is a locus that can reach the imaginary axis twice with the given range of Φ. Here, the reactive power located in the top half part of the locus is used with the range of the outer phase shift Φ $(0, \pi/2)$. By comparing those control methods, it is clear that the increase of the inner phase shift θ_1 and θ_2 has a negative influence on the maximum active power transmission ability. Under the specified parameters, SPS has larger maximum transmission power than EPS1 and EPS2, DPS has the lowest power among all the control strategies, while SPS and POPS can reach the maximum unified active power $P = 1$. According to Fig. 9(a), EPS1, DPS, and POPS have lower reactive power than SPS, in which POPS has the lowest reactive power. In light load condition, when P is less than 0.55, the reactive power of the POPS control is equal to zero. Fig. 9(b) is the reactive power varied with the voltage conversion ratio k when the active power $P = 0.6$. For EPS, DPS, and SPS control, the reactive power is increasing linear with the increase of k. Compared with those methods, POPS can significantly reduce the reactive power in any voltage conversion ratio k condition, especially for the higher k condition.

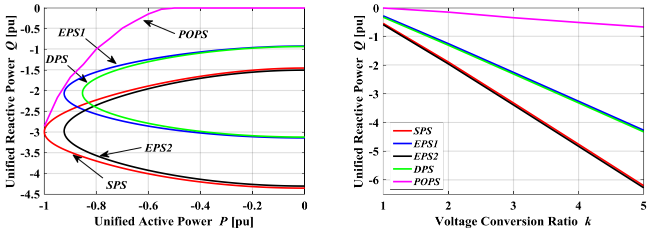

(a) (b)

Fig. 10. (a) Phasor diagrams of the negative direction apparent power for different control method when $k = 2$. (b) Reactive power of different control method when $P = -0.6$ varied with voltage conversion ratio k.

In order to investigate the bidirectional power flow ability, the reverse operation mode of the DAB converter is shown in Fig. 10. It can be seen that the reactive power varied with positive direction transmission power P and the voltage conversion ratio k are the same as the forward power flow mode. The reactive power is increasing along with the unified active power and voltage conversion ratio, while the POPS has the lowest reactive power. So, it proves that POPS is not only suitable for the forward power flow condition, but also available for the reverse operation mode.

Fig. 11(a) shows the changes of phase shift varied with the unified active power. It can be seen that the primary and secondary inner phase shift θ_1, θ_2 are decreasing along with the increasing active power P, while the outer phase shift ϕ is always maintained around 1.5 rad. The secondary inner phase shift θ_2 drops much faster than primary inner phase shift θ_1 and reach zero when $P = 0.55$. When the active transmission power $P = 1$, POPS has phase shift $\theta_1 = 0, \theta_2 = 0, \phi = \pi/2$ which is same as SPS control. Fig. 11(b) indicates that both θ_1 and ϕ

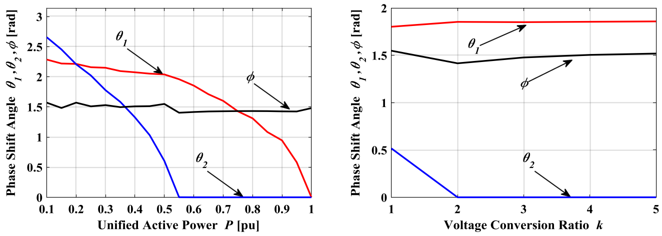

(a) (b)

Fig. 11. (a) Phase shift variations with the unified active power under buck mode. (b) Phase shift variations with voltage conversion ratio k under buck mode.

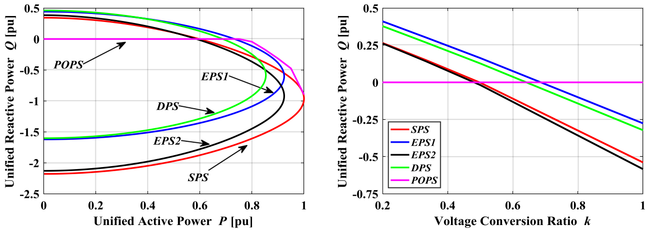

(a) (b)

Fig. 12. (a) Phasor diagrams of the positive direction apparent power for different control methods when $k = 1/2$. (b) Reactive power of different control methods when $P = 0.4$ varied with voltage conversion ratio k.

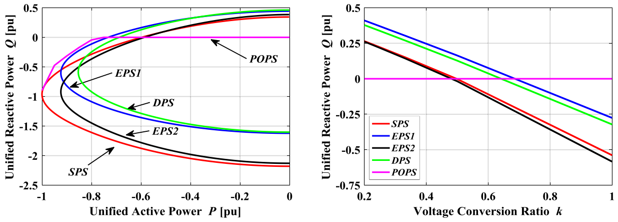

(a) (b)

Fig. 13. (a) Phasor diagrams of the negative direction apparent power for different control methods when $k = 1/2$. (b) Reactive power of different control methods when $P = 0.6$ varied with voltage conversion ratio k.

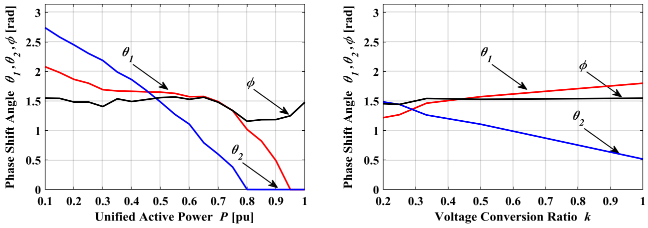

Fig. 14. (a) Phase shift variations with the unified active power under boost mode. (b) Phase shift variations with voltage conversion ratio k under boost mode.

are maintaining stable when θ_2 is rapidly decreasing to the zero during the increasing of the voltage conversion ratio k.

Under the boost mode with the voltage conversion ratio $k = 1/2$, main results are illustrated in Figs. 12–14. Under the buck mode, the reactive power is always in the negative direction, as illustrated in Fig. 8. However, under the boost mode, the reactive power exists in both positive and negative directions. Thus, the direction may affect the searching of the minimum reactive power and the absolute value of the fitness function $Q(\theta_1, \theta_2, \phi)$ has been used to avoid the influence of direction change. The comparison among SPS, EPS1, EPS2, DPS, and POPS under boost mode shows different results from those under the buck mode. When the unified reactive power P < 0.6, the reactive power is located on the positive half axis. EPS1 and DPS clearly have larger positive reactive power than SPS and EPS2. However, when reactive power is located in the negative half axis, EPS1 and DPS have less reactive power than SPS and EPS2. It indicates that the fixed-inner-phase-shift methods like EPS1 and DPS under buck mode may not guarantee a reactive reduction especially for the light load condition. Fig. 12(a) shows that POPS can ensure the lowest reactive power operation under all load conditions. Furthermore, POPS can be stable at zero reactive power before $P = 0.8$. The relationship between reactive power and voltage conversion ratio is shown in Fig. 12(b). When the reactive power is in the positive direction, the increasing k will lead to the decreasing reactive power and the SPS has lower reactive power than EPS1 and DPS. For the negative direction reactive power, as illustrated in Fig. 13, the increasing k will lead to the rising reactive power and the SPS has larger reactive power than EPS1 and DPS. For given operation condition $P = 0.6$ and $k = 1/2$, POPS can ensure zero reactive power. The changes of phase shifts θ_1, θ_2, ϕ varied with P and k under buck mode are illustrated in Fig. 14. The center phase shift ϕ is around 1.5 rad, while θ_1, θ_2 are rapidly reducing to zero. For the voltage conversion ratio variation condition, ϕ is stable at the 1.5 rad. The primary inner phase shift θ_1 is increasing with the rising k, while the secondary inner phase shift θ_2 is decreasing with the rising k.

D. Soft Switching Boundary Analysis by Unified Phasor Diagram

In order to investigate the zero voltage switching (ZVS) boundary of all switches, the inductor current for each switch turning ON the moment is required. In the DAB converter, it has four switches S_1–S_4 on the primary-side full bridge and Q_1–Q_4 on the secondary-side full bridge. Those switches can be divided into four switches pair: $S_{1,2}$, $S_{3,4}$, $Q_{1,2}$, and $Q_{3,4}$ because complementary switches on the same bridge arm have the same ZVS boundary. According to the principle of the ZVS, the soft-switching boundary conditions are expressed as

$$\begin{aligned} S_{3,4} &: I_L(\omega_0 t = \theta_1/2) \leq 0 \\ S_{1,2} &: I_L(\omega_0 t = \pi - \theta_1/2) \geq 0 \\ Q_{3,4} &: I_L(\omega_0 t = \phi + \theta_2/2) \geq 0 \\ Q_{1,2} &: I_L(\omega_0 t = \pi + \delta - \theta_2/2) \leq 0. \end{aligned} \tag{20}$$

After combining inductor current constraint of the ZVS in (20) and inductor current equation in (4), ZVS boundary for each switches pairs can be expressed as (21) shown at the bottom of the next page. According to (21), the ZVS boundary of four switches pairs can be expressed as the maximum and minimum value of the voltage conversion ratio k, which can be calculated by the given inner phase shift θ_1, θ_2 and center point phase shift ϕ. When the operation voltage conversion ratio k is larger than the calculated primary ZVS boundary, the primary

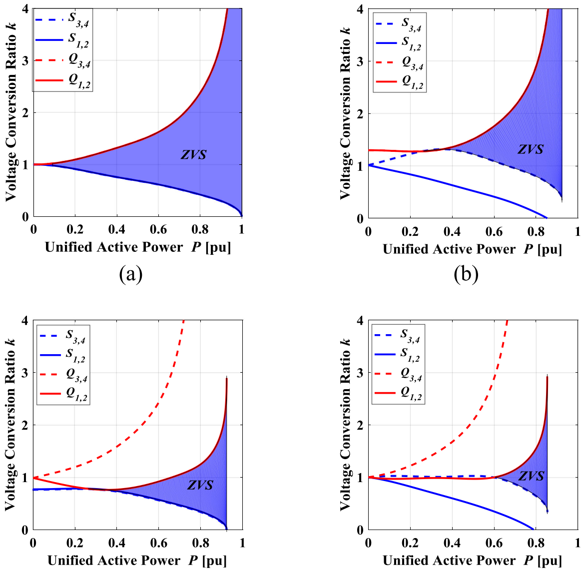

(a) (b) (c) (d)

Fig. 15. (a) ZVS region for $\theta_1 = 0, \theta_2 = 0$ under SPS control. (b) ZVS region for $\theta_1 = \pi/4, \theta_2 = 0$ under EPS1 control. (c) ZVS region for$\theta_1 = 0, \theta_2 = \pi/4$ under EPS2 control. (d) ZVS region for $\theta_1 = \pi/4, \theta_2 = \pi/4$ under DPS control.

side switches S_1–S_4, can turn ON as soft switching. When the operation voltage conversion ratio k is lower than calculated secondary ZVS boundary, the secondary side switches Q_1–Q_4, can turn ON as soft switching.

As shown in Fig. 15, the ZVS boundary of each switch pairs varied with unified active power P is presented and the full ZVS region is marked by blue area. It is clear that a larger transmission power can extend ZVS region and the inner phase shift θ_1, θ_2 has an obvious influence on the ZVS boundary of all switch pairs. For the SPS control, it can ensure soft switching for all switches under all load conditions when $k = 1$. In Fig. 15(b), EPS1 with inner phase shift $\theta_1 = \pi/4$ significantly raises the ZVS boundary of switches S_3 and S_4, while slightly extending ZVS boundaries of $S_{1,2}$, $Q_{1,2}$, and $Q_{3,4}$ switches. It indicates that EPS1 can easily achieve zero-voltage switching under high-voltage conversion condition than SPS control. The influence of secondary inner phase shift θ_2 is shown in Fig. 15(c). EPS2 narrows the ZVS boundary of $Q_{1,2}$, while slightly extends ZVS boundaries of $S_{1,2}$, $S_{3,4}$, and $Q_{3,4}$. So it can ensure larger fully soft switching under lower k conditions than SPS control. Due to the primary and secondary inner phase shift, DPS control can extend ZVS boundary of $S_{1,2}$ and $Q_{1,2}$, but the overall ZVS region is dramatically reduced under various k conditions.

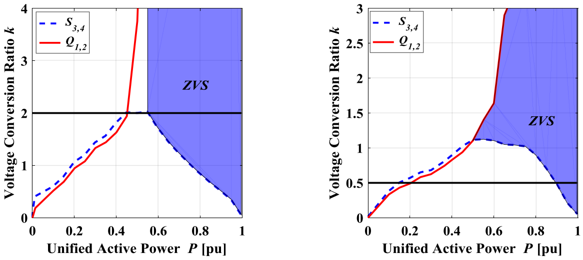

(a) (b)

Fig. 16. (a) ZVS region under POPS control when $k = 2$. (b) ZVS region under POPS control when $k = 1/2$.

The ZVS boundary of the POPS control for $k = 2$ and $k = 1/2$ are shown in Fig. 16. Because the ZVS boundary condition of $S_{1,2}$ and $Q_{3,4}$ can always achieve in the POPS control, so the overall ZVS region depends on the ZVS boundary of $S_{3,4}$ and $Q_{1,2}$. According to Fig. 16(a), the ZVS condition of the POPS under $k = 2$ can be divided into three different conditions varied with transmission power. When the transmission power P belongs to 0 to 0.45, the $S_{3,4}$ can achieve soft switching and the $Q_{1,2}$ acts as hard switching. The secondary ZVS condition occurs during $P = 0.45$ to $P = 0.55$, the $Q_{1,2}$ can ensure soft switching condition while the $S_{3,4}$ becomes hard switching operation state. The final condition is that POSP can ensure soft switching of all switches when the transmission power is larger than 0.55. Based on the above analysis, it is clear that POPS can ensure at least three switch pairs—$S_{1,2}$, $Q_{3,4}$, and $S_{3,4}$ or $Q_{1,2}$ achieve zero-voltage switching, and achieve full ZVS operation since transmission power P is larger than 0.55. Fig. 16(b) shows the corresponding analysis for the boost mode. Compared with ZVS region of SPS, EPS1, EPS2, and DPS, the proposed POPS under $k = 2$ can achieve an additional switching pairs in the light load and larger full ZVS operation region sin $P = 0.55$.

IV. EXPERIMENTAL RESULTS

A. *Experimental Prototype*

In order to verify the theoretical analysis, a prototype of DAB converter was built and main parameters are listed in Table I. The SPS, EPS, and POPS control methods were implemented

---

$$\begin{cases} k\left(\sum\limits_{n=1,3,5,..} \dfrac{4\cos^2(n\alpha/2)}{n^2\pi\omega_0 L}\right) \geq \sum\limits_{n=1,3,5,..} \dfrac{4\cos(n\beta/2)}{n^2\pi\omega_0 L}\left[\sin(n\alpha/2)\sin(n\delta) + \cos(n\alpha/2)\cos(n\delta)\right] \\ k\left(\sum\limits_{n=1,3,5,..} \dfrac{4\cos^2(n\alpha/2)}{n^2\pi\omega_0 L}\right) \geq \sum\limits_{n=1,3,5,..} \dfrac{4\cos(n\beta/2)}{n^2\pi\omega_0 L}\left[\cos(n\alpha/2)\cos(n\delta) - \sin(n\alpha/2)\sin(n\delta)\right] \\ k\left(\sum\limits_{n=1,3,5,..} \dfrac{4\cos(n\delta+n\beta/2)\cos(n\alpha/2)}{n^2\pi\omega_0 L}\right) \leq \sum\limits_{n=1,3,5,..} \dfrac{4\cos(n\beta/2)}{n^2\pi\omega_0 L}\left[\sin(n\delta+n\beta/2)\sin(n\delta) + \cos(n\delta+n\beta/2)\cos(n\delta)\right] \\ k\left(\sum\limits_{n=1,3,5,..} \dfrac{4\cos(n\delta-n\beta/2)\cos(n\alpha/2)}{n^2\pi\omega_0 L}\right) \leq \sum\limits_{n=1,3,5,..} \dfrac{4\cos(n\beta/2)}{n^2\pi\omega_0 L}\left[\sin(n\delta-n\beta/2)\sin(n\delta) + \cos(n\delta-n\beta/2)\cos(n\delta)\right] \end{cases} \quad (21)$$

TABLE I
PARAMETERS OF THE DAB CONVERTER PROTOTYPE

Item	Parameter
Transformer turns ratio N	2
Inductance L_s	60 μH
Switching frequency f	20 kHz
Maximum input voltage V_{in}	200 V
Maximum output voltage V_{out}	200 V

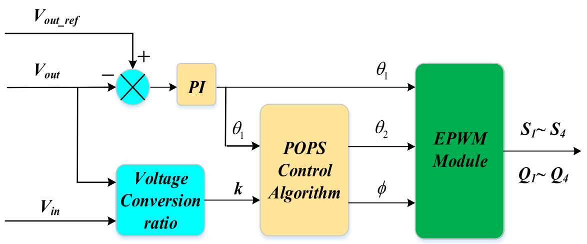

Fig. 17. Control implementation of the POPS algorithm.

TABLE II
COMPARISON OF THE EXECUTION TIME IN DSP CONTROLLER

Control	Time (cycle)	Time (ms)
Open-loop control	755906	5.039
Proposed POPS control (With initialization)	762 761	5.085
Proposed POPS control (After initialization)	1057	0.007

in DSP28335 and applied to the built prototype for evaluation. The performance in terms of reactive power and efficiency was investigated for a wide input voltage range and different load conditions.

B. *Control Implementation*

Fig. 17 illustrates the implementation diagram of the proposed POPS control algorithm for the experiments by using the DSP TMS320F28335. The PI voltage controller was used to regulate the output voltage with its output as the primary inner phase shift variable θ_1. The PSO algorithm was implemented in an offline manner by using the method of lookup table. Specifically, the input variables of POPS algorithm are the primary inner phase shift variable θ_1 from the output voltage PI controller and the voltage conversion ratio k. The output variables of POPS algorithm are the secondary inner phase shift variable θ_2 and outer phase shift variable ϕ. POPS can obtain the optimal variables of θ_2 and ϕ, which were stored in a numeric table and loaded into the DSP board. Then, the enhanced pulse width modulator (EPWM) module was used to generate gate signal for switches $S_1 \sim S_4$ and $Q_1 \sim Q_4$. Since the proposed control scheme requires only two voltage sensors to measure the input and output voltage, the cost is low since there is no expensive current sensor needed.

Table II shows the measured computation cycle and time with the proposed algorithm in DSP in order to evaluate the computation burden. Both the open-loop and the closed-loop controls with POPS algorithm were implemented and their execution time was recorded by using the interrupt timing function of DSP board TMS320F28335. Considering that the POPS algorithm was implemented in an offline manner, relative long initialization is required to load the calculated numerical table into the DSP board. Thus, Table II lists the measures, cycles, and time for both the proposed POPS algorithm with initialization and after initialization. It shows that extra 6855 cycles or 46 μs were required to implement the proposed POPS with initialization compared with that of the open-loop control. The total measured increase of the execution time was just 1% of that with the open-loop control. Furthermore, since the initialization process will be executed just one time for the table loading into the DPS board, the real execution time for the POPS algorithm after initialization is 1057 duty cycles, which is 7 μs. Since the switching period of the DAB converter is 50 μs according to Table I, the required time for running POPS control after initialization is much less than the switching period. Thus, the computation burden increases when the proposed algorithm is low.

C. *Verification of the Harmonic Phasor Analysis*

The experimental and theoretical waveforms by the proposed phasor expression for SPS, EPS, and DPS control when $V_{\text{in}} = 75$ V and $V_{\text{out}} = 75$ V are shown in Fig. 18. Based on those figures, it is clear that the theoretical waveforms based on the harmonicas analysis well match the experimental waveforms for different control strategies. It demonstrates that the harmonics phasor analysis is accurate enough to represent the operation status of the DAB converter with all control methods.

D. *Steady-State Experimental Results*

First, the forward and buck operation is evaluated. Fig. 19 shows experimental waveforms of SPS, EPS with "$\theta_1 = \pi/4$," and POPS control when $k = 2$ and $P = 1200$ W. The reactive power is represented by the opposite direction current and voltage since this part current will be circulating inside the input or output side bridge. From the waveforms of SPS and EPS, it is clear that both have obvious reactive power, while the SPS has larger reactive power than EPS. On the contrary, POPS can obviously eliminate the reactive power with the same transmission power because the larger inner phase shift angle θ_1 of POPS can significantly reduce the backflow current, and then reduce the overall reactive power. For ZVS operation, different colors are used in Fig. 19 for different switches. Specifically, blue dotted circle represents the ZVS for $S_{3,4}$. Similarly, blue circle represents the ZVS for $S_{1,2}$, red dotted circle represents the ZVS for $Q_{3,4}$, and red circle represents the ZVS for $Q_{3,4}$. Fig. 19 shows that under the heavy load condition, SPS control can only ensure primary switches $S_{1,2}$ and $S_{3,4}$, while EPS and POPS can achieve soft switching of all switches. Compared ZVS boundary of EPS, it is clear that POPS has a larger margin for soft switching.

Main experimental waveforms of SPS, EPS, and POPS under $k = 2$ and light-load condition of "$P = 600$ W" are shown in Fig. 20. It can be seen that the reactive power under light load condition still exists in the DAB converter for both EPS and SPS,

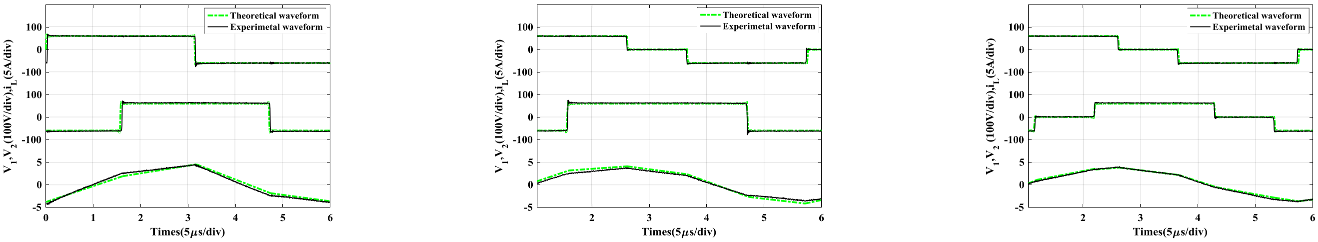

(a) (b) (c)

Fig. 18. Comparison of the theoretical and experimental waveforms under different control methods. (a) SPS. (b) EPS. (c) DPS.

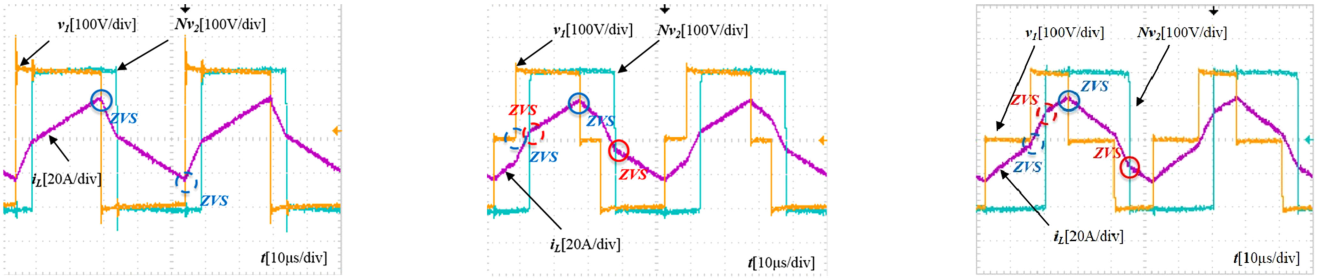

(a) (b) (c)

Fig. 19. Experimental waveforms for the forward, buck mode, and heavy-load condition: $V_{\mathrm{in}} = 200$ V, $V_{\mathrm{out}} = 200$ V, and $P = 1200$ W. (a) SPS control. (b) EPS control. (c) POPS control.

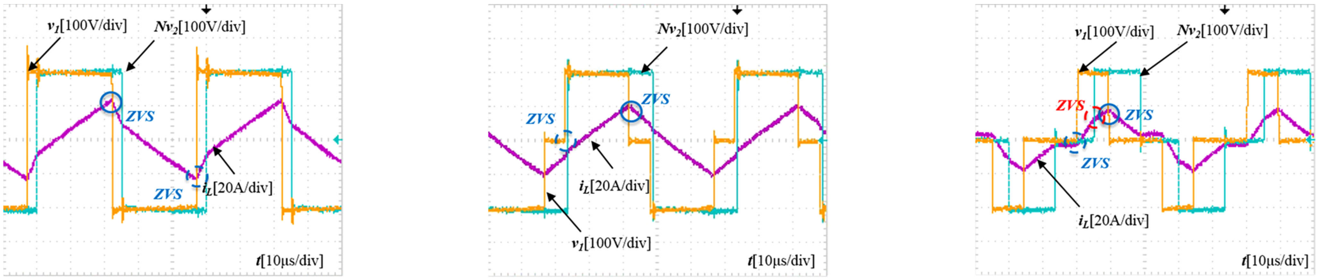

(a) (b) (c)

Fig. 20. Experimental waveforms for the forward, buck mode, and light-load condition: $V_{\mathrm{in}} = 200$ V, $V_{\mathrm{out}} = 200$ V, and $P = 600$ W. (a) SPS control. (b) EPS control. (c) POPS control.

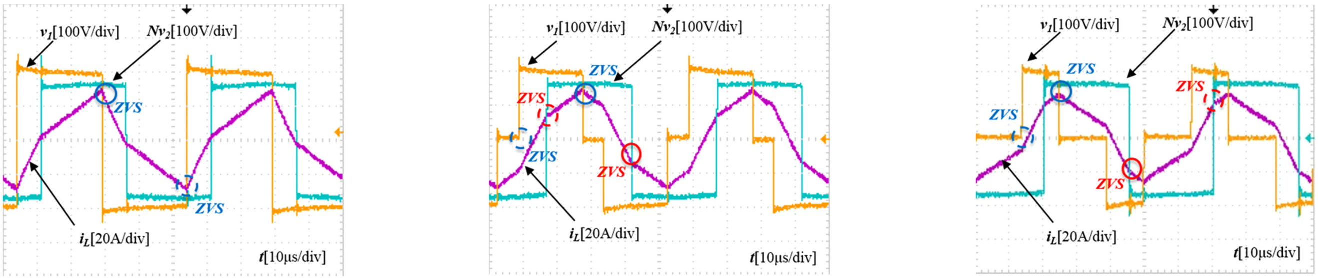

(a) (b) (c)

Fig. 21. Experiment waveform for the forward, buck mode (larger k), and heavy-load condition: $V_{\mathrm{in}} = 200$ V, $V_{\mathrm{out}} = 160$ V, and $P = 1200$ W. (a) SPS control. (b) EPS control. (c) POPS control.

which can cause addition reactive power and reduce efficiency. However, POPS control can also eliminate the backflow current and ensure lower reactive power under the light load condition. Compared with heavy load condition in Fig. 19(c), POPS in the light load condition modifies both the primary and secondary inner phase shift θ_1 and θ_2 in order to achieve better reactive power reduction performance. Under the light load condition, POPS can ensure six switches S_1–S_4 and Q_3–Q_4 operating as ZVS soft switching, while the EPS and SPS only have primary side switches S_1–S_4 under ZVS.

The performance of SPS, EPS, and POPS under a larger voltage conversion condition $k = 2.5$ and $P = 1200$ W are evaluated and main experimental results are shown in Fig. 21. Compared with those waveforms under $k = 2$ in Fig. 19, it can be

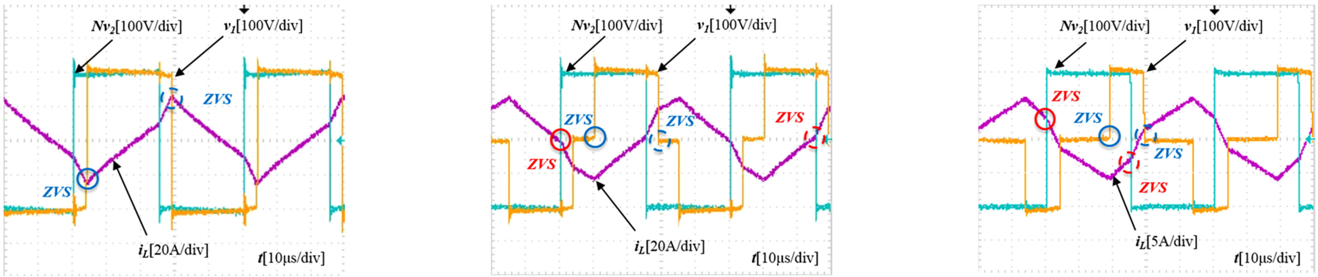

(a) (b) (c)

Fig. 22. Experiment waveforms for the reversve, buck mode, and heavy-load condition: $V_{\rm in} = 200$ V, $V_{\rm out} = 200$ V, and $P = 1200$ W. (a) SPS control. (b) EPS control. (c) POPS control.

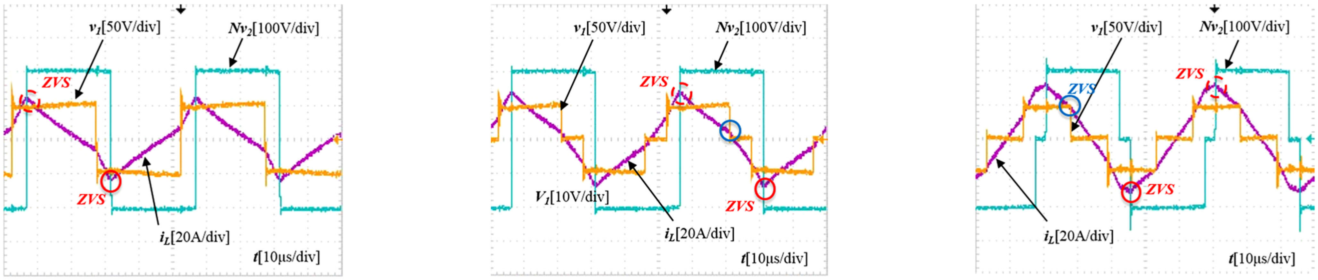

(a) (b) (c)

Fig. 23. Experiment waveforms for the forward, boost mode and heavy-load condition: $V_{\rm in} = 50$V, $V_{\rm out} = 200$ V, and $P = 300$ W. (a) SPS control. (b) EPS control. (c) POPS control.

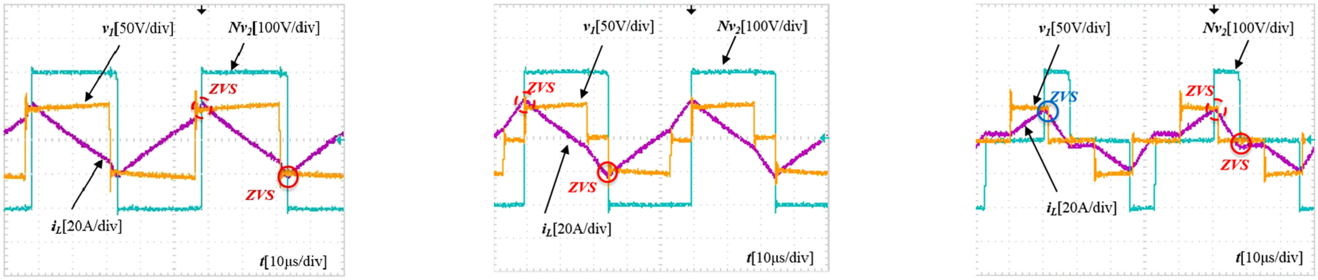

(a) (b) (c)

Fig. 24. Experiment waveforms for the forward, boost mode, and light-load condition: $V_{\rm in} = 50$ V, $V_{\rm out} = 200$ V, and $P = 150$ W. (a) SPS control. (b) EPS control. (c) POPS control.

seen that the reactive power under all control methods is increasing. It proves the theoretical analysis that increasing voltage conversion ratio can lead to larger reactive power. In the same time, SPS can only achieve ZVS on primary side switches, while both EPS and POPS can achieve ZVS for all switches.

The experimental waveforms for the reverse, buck mode, and heavy-load condition with SPS, EPS, and POPS under $k = 2$ and $P = 1200$ W are shown in Fig. 22. Compared with the forward mode, as illustrated in Fig. 19, the waveforms of reverse mode are similar, including both the ZVS and backflow power performance. Among all the control methods, POPS clearly has the least reactive power than others.

The experimental DAB converter for the boost operation is also evaluated. Fig. 23 shows main experimental waveforms for the boost mode when $k = 0.5$ and $P = 300$ W. It can be seen that both EPS and POPS can eliminate the backflow current and achieve ZVS on six switches. However, POPS has a larger margin for ZVS boundary of $S_{3,4}$ which can ensure ZVS under lower-load condition. As illustrated in Fig. 24, under the light-load condition, POPS can ensure $S_{1,2}$, $Q_{1,2}$, and $Q_{3,4}$ operating as soft switching, while SPS and EPS can only ensure $Q_{1,2}$ and $Q_{3,4}$ under ZVS.

Fig. 25 shows the experimental results for a larger mismatch voltage condition $k = 1/3$ and $P = 300$ W when input voltage $V_{\rm in} = 50$ V and output voltage $V_{\rm out} = 200$ V. It can be seen that the backflow current using SPS is significantly increasing. Although EPS and POPS still reduce the reactive power to some extent, especially the input-side reactive power, verification of the harmonic phasor analysis in the output-side reactive power cannot be eliminated. Furthermore, compared with the buck mode, the DAB converter using the POPS shows higher reactive power and smaller ZVS region.

Fig. 26 shows the comparison of reactive power using different control methods, including SPS, EPS, and DPS, the proposed POPS, and the minimum rms current phase shift control (MPS) proposed in [11]. For the buck mode "$k = 2$," as

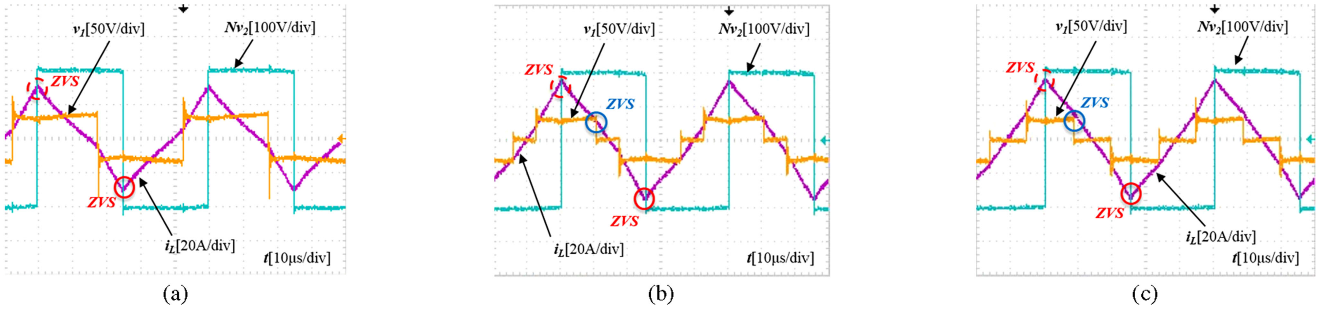

Fig. 25. Experiment waveforms for the forward, boost mode (smaller k) and heavy-load condition: $V_{\text{in}} = 33.3$ V, $V_{\text{out}} = 200$ V and $P = 300$ W. (a) SPS control. (b) EPS control. (c) POPS control.

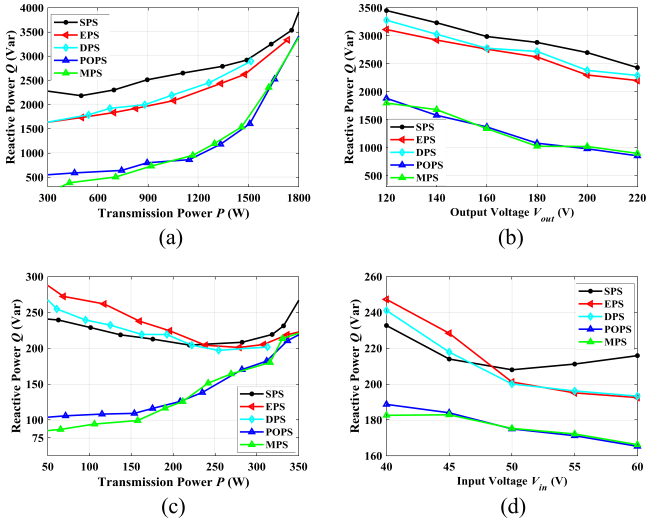

Fig. 26. (a) Reactive power Q under various control methods varied with transmission power P when $V_{\text{in}} = 200$ V, $V_{\text{out}} = 200$ V. (b) Reactive power Q varied with output voltage V_{out} when $P = 1200$ W, $V_{\text{in}} = 200$ V. (c) Reactive power Q under various control methods varied with transmission power P when $V_{\text{in}} = 50$ V, $V_{\text{out}} = 200$ V. (d) Reactive power Q varied with input voltage V_{in} when $P = 300$ W, $V_{\text{out}} = 200$ V.

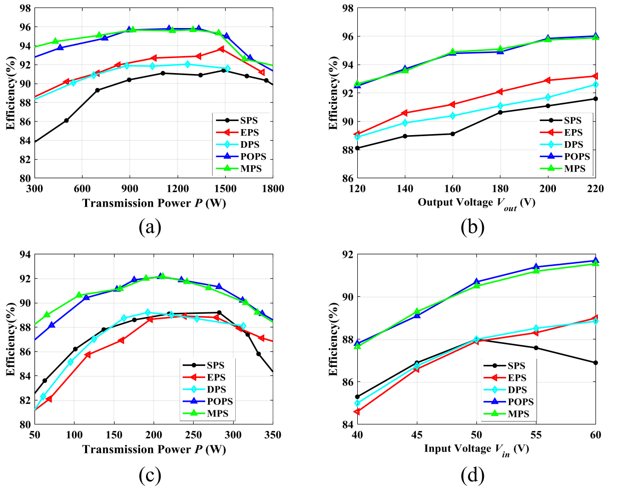

Fig. 27. (a) Efficiency under various control methods varied with transmission power P when $V_{\text{in}} = 200$ V, $V_{\text{out}} = 200$ V. (b) Efficiency varied with output voltage V_{out} when $P = 1200$ W, $V_{\text{in}} = 200$ V. (c) Efficiency under various control methods varied with transmission power P when $V_{\text{in}} = 50$ V, $V_{\text{out}} = 200$ V. (d) Efficiency varied with input voltage V_{in} when $P = 300$ W, $V_{\text{out}} = 200$ V.

illustrated in Fig. 26(a), the input voltage and output voltage maintain at 200 V and transmission power is changing from 300 to 1800 W. Fig. 26(a) indicates that POPS and MPS show very similar performance in minimizing the reactive power for the whole range of the transmission power. Actually each of them can be regarded as the best strategy for the reactive power reduction among all these strategies. EPS has less reactive power than DPS and SPS control. However, the difference of reactive power among all control strategies is decreasing along with the increasing P, the reactive power of POPS and MPS is almost equal to the reactive power of SPS when the transmission power is equal to 1800 W. Fig. 26(b) shows that reactive power varied with different output voltage NV_2 when input voltage V_{in} is stable as 200 V and transmission power is stable as 1200 W. It is clear that reactive power for all control strategies is decreasing with rising output voltage V_{out}. For each voltage conversion ratio k condition, the reactive power under EPS is slightly less than SPS and DPS, while the POPS and MPS has the lowest reactive power. The reactive power of MPS and POPS is very similar, while MPS has slightly lower reactive power than POPS control at light load condition. This experimental result support above theoretical analysis about the changes of reactive power varied with k.

Fig. 26(c) and (d) illustrates the corresponding reactive power for boost mode when $k = 1/2$. Fig. 26(c) shows changes of reactive power of different control methods under boost mode when transmission power is varied from 50 to 350 W with input voltage $V_{\text{in}} = 50$ V and output voltage $V_{\text{out}} = 200$ V. The reactive power varied with transmission power P can be divided into two cases determined by different P. Case 1: when the P is less than 220 W, EPS has largest reactive power and DPS has larger reactive power than SPS control. Furthermore, the reactive power for all methods is decreasing with larger active power. The difference of reactive power is reducing along with increasing active power. Case 2: when P is larger than 220 W, the relationship between active and reactive power will reverse, the reactive power is increasing with raising active power and the EPS has less reactive power than SPS and DPS control. The main reason for two different cases is the change of reactive power direction, which has been analyzed and illustrated in Fig. 12. The reactive power varied with active power is first decreasing before P is equal to 220 W and then increasing when P is larger than 220 W. For any case, POPS and MPS can achieve

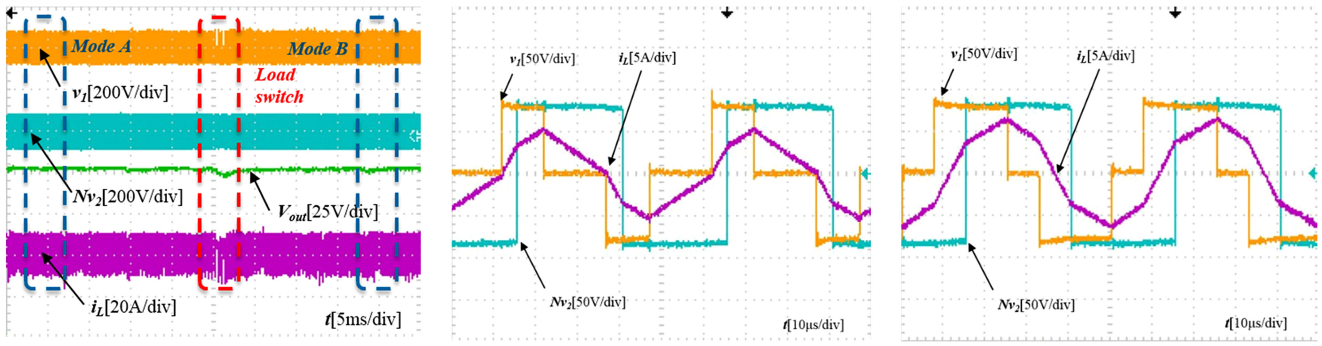

(a) (b) (c)

Fig. 28. (a) Experimental waveforms for the load change condition with $V_{\text{in}} = 80$ V and $V_{\text{out}} = 80$ V. (b) Experimental waveforms of mode A with the 32 Ω load resistance. (c) Experimental waveforms of mode B with the 21.4 Ω load resistance.

minimum reactive power for all load conditions, while MPS has slightly lower reactive power than POPS control. The reactive power varied with input voltage V_{in} when output voltage V_{out} is equal to 200 V and transmission power P is maintained as 300 W in Fig. 26(d). It indicates that POPS and MPS have the lowest reactive power for any voltage conversion ratio k.

Fig. 27(a) shows the curves of efficiencies for $k = 2$ condition varied with transmission power when $V_{\text{in}} = 200$ V and output voltage $V_{\text{out}} = 200$ V. The measued efficiencies of EPS and DPS are higher than SPS control for all load conditions, while the efficiencies of EPS and DPS are very similar. Under all load conditions, POPS and MPS have very similar efficiency which is higher than other controls, while MPS has slightly higher efficiency than POPS control in light-load condition. POPS and MPS have maximum efficiency, about 96% around 1300 W. Compared with SPS, the experimental results show that the maximum efficiency for POPS under the rated load is improved by 5% and the efficiency improvement under the light-load condition is 9%. Curves of efficiency varied with the voltage conversion ratio k when $V_{\text{in}} = 200$ V and $P = 1200$ W. It shows that efficiency of all control methods are improved with larger output voltage V_{out}. The rank of the measured efficiencies under all k conditions is POPS and MPS, EPS, DPS, and SPS. According to the comparison result in Fig. 27(a) and (b), it is clear that POPS and MPS can achieve the highest efficiency, which agrees above theoretical and experimental result of reactive power analysis.

The measured efficiencies of SPS, EPS, DPS, POPS, and MPS under $k = 1/2$ condition are shown in Fig. 27(c) and (d). Similar to the control methods under $k = 2$ condition, POPS and MPS can ensure the best efficiency in all load conditions and reach maximum efficiency about 92% when $P = 200$ W. Compared with other strategies, the experimental results show that the maximum efficiency under the rated load is improved by 3% and the efficiency improvement under the light-load condition is high up to 5%. Fig. 27(d) indicates that the measured efficiencies of EPS and DPS are increasing with transmission power and significantly higher than SPS when the input voltage is larger than 50 V. The comparison of efficiency also shows that POPS and MPS always have higher efficiency than other strategies. Based on above analysis, it can be seen that POPS has very similar performance as MPS control, while MPS can slightly reduce reactive power and improve efficiency in light load condition. It may be because the nonreactive operation state of POPS in light-load condition is determined by ideal model of switches, inductor, and transformer. So additional parameter like resistance of transformer will affect the nonreactive operation states. It may improve by introducing real model instead of ideal model in future work. The advantage of POPS control based on harmonic analysis and PSO algorithm is that it can significantly reduce workload for searching optimization control algorithm. Also, it can be easily adapted to different models and optimization target.

E. Dynamic Experimental Results

Fig. 28 shows main experiment results for the load changing condition. Specifically, the load resistance is changing from 32 to 21.4 Ω, while both V_{in} and V_{out} are fixed at 80 V. At the beginning, the output voltage V_{out} slightly dropped due to the change of the load resistance. Then, it was observed that V_{out} was quickly returning to stable at the required voltage level as 80 V. It validates the correct operation of the output voltage closed-loop control and also fast dynamic performance of the POPS algorithm. Furthermore, waveforms for modes A and B were zoomed and illustrated in Fig. 28(b) and (c), which prove the effectiveness of the POPS optimization algorithm for different load conditions.

V. CONCLUSION

This paper proposes POPS based on the unified phasor analysis with the aim to minimize the reactive power and improve the efficiency of the bidirectional DAB converter for the whole operation range. First, through building a unified mathematical model based on Fourier transform for the DAB converter, accurate complex mathematical expressions for the inductor current, the transmission power, and the reactive power are obtained. Then, the unified-phasor-based PSO is adopted to directly determine the optimal phase-shift variables in minimizing the reactive power under three-level modulated phase shift control without a cumbersome process of the optimal operation mode selection. Main analysis and experimental results are provided for different voltage conversion ratio and load conditions. Various modes, including forward mode, reverse mode, buck mode, and boost mode, are also analyzed. The results show that the proposed POPS can successfully minimize the reactive power and maintain a high maximum transmission power especially in the high voltage conversion and light-load condition. Furthermore, the ZVS region is extended using POPS, which can reduce switching loss. Specifically, with the proposed POPS algorithm, the measured maximum efficiency under the rated load is improved by 3% and the efficiency improvement under the light-load condition is high up to 9%. The dynamic test result under the load changing condition validate the correct operation of the output voltage closed-loop control and fast dynamic response of the proposed POPS algorithm.

REFERENCES

[1] B. Zhao, Q. Song, W. Liu, and Y. Sun, "Overview of dual-active-bridge isolated bidirectional DC-DC converter for high-frequency-link power-conversion system," *IEEE Trans. Power Electron.*, vol. 29, no. 8, pp. 4091–4106, Aug. 2014.

[2] F. Krismer and J. W. Kolar, "Accurate power loss model derivation of a high-current dual active bridge converter for an automotive application," *IEEE Trans. Ind. Electron.*, vol. 57, no. 3, pp. 881–891, Mar. 2010.

[3] Y. Xie, J. Sun, and J. S. Freudenberg, "Power flow characterization of a bidirectional galvanically isolated high-power DC/DC converter over a wide operating range," *IEEE Trans. Power Electron.*, vol. 25, no. 1, pp. 54–66, Jan. 2010.

[4] H. Wen, B. Su, and W. Xiao, "Design and performance evaluation of a bidirectional isolated dc-dc converter with extended dual-phaseshift scheme," *IET Power Electron.*, vol. 6, no. 5, pp. 914–924, May 2013.

[5] Y. Shi, R. Li, Y. Xue, and H. Li, "Optimized operation of current-fed dual active bridge DC-DC converter for PV applications," *IEEE Trans. Ind. Electron.*, vol. 62, no. 11, pp. 6986–6995, Nov. 2015.

[6] G. Xu, D. Sha, J. Zhang, and X. Liao, "Unified boundary trapezoidal modulation control utilizing fixed duty cycle compensation and magnetizing current design for dual active bridge DC–DC converter," *IEEE Trans. Power Electron.*, vol. 32, no. 3, pp. 2243–2252, Mar. 2017.

[7] H. Wen, W. Xiao, and B. Su, "Nonactive power loss minimization in a bidirectional isolated DC–DC converter for distributed power systems," *IEEE Trans. Ind. Electron.*, vol. 61, no. 12, pp. 6822–6831, Dec. 2014.

[8] H. Wen and B. Su, "Operating modes and practical power flow analysis of bidirectional isolated power interface for distributed power systems," *Energy Convers. Manage.*, vol. 111, pp. 229–238, 2016.

[9] C. Mi, H. Bai, C. Wang, and S. Gargies, "Operation, design and control of dual H-bridge-based isolated bidirectional DC–DC converter," *IET Power Electron.*, vol. 1, no. 4, pp. 507–517, 2008.

[10] A. Rodríguez, A. Vázquez, D. G. Lamar, M. M. Hernando, and J. Sebastián, "Different purpose design strategies and techniques to improve the performance of a dual active bridge with phase-shift control," *IEEE Trans. Power Electron.*, vol. 30, no. 2, pp. 790–804, Feb. 2015.

[11] A. Tong, L. Hang, G. Li, X. Jiang, and S. Gao, "Modeling and analysis of dual-active-bridge isolated bidirectional DC/DC converter to minimize RMS current," *IEEE Trans. Power Electron.*, vol. 33, no. 6, pp. 5302–5316, Jun. 2018.

[12] D. Costinett, D. Maksimovic, and R. Zane, "Design and control for high efficiency in high step-down dual active bridge converters operating at high switching frequency," *IEEE Trans. Power Electron.*, vol. 28, no. 8, pp. 3931–3940, Aug. 2013.

[13] G. Oggier, G. O. Garc, and A. R. Oliva, "Modulation strategy to operate the dual active bridge DC-DC converter under soft switching in the whole operating range," *IEEE Trans. Power Electron.*, vol. 26, no. 4, pp. 1228–1236, Apr. 2011.

[14] F. Krismer, S. Round, and J. W. Kolar, "Performance optimization of a high current dual active bridge with a wide operating voltage range," in *Proc. 37th IEEE Power Electron. Spec. Conf.*, 2006, pp. 1–7.

[15] G. G. Oggier, G. O. Garc, and A. R. Oliva, "Switching control strategy to minimize dual active bridge converter losses," *IEEE Trans. Power Electron.*, vol. 24, no. 7, pp. 1826–1838, Jul. 2009.

[16] A. K. Jain and R. Ayyanar, "PWM control of dual active bridge: Comprehensive analysis and experimental verification," *IEEE Trans. Power Electron.*, vol. 26, no. 4, pp. 1215–1227, Apr. 2011.

[17] B. Zhao, Q. Yu, and W. Sun, "Extended-phase-shift control of isolated bidirectional DC-DC converter for power distribution in microgrid," *IEEE Trans. Power Electron.*, vol. 27, no. 11, pp. 4667–4680, Nov. 2012.

[18] H. Bai and C. Mi, "Eliminate reactive power and increase system efficiency of isolated bidirectional dual-active-bridge DC-DC converters using novel dual-phase-shift control," *IEEE Trans. Power Electron.*, vol. 23, no. 6, pp. 2905–2914, Nov. 2008.

[19] S. S. Muthuraj, V. K. Kanakesh, P. Das, and S. K. Panda, "Triple phase shift control of an LLL tank based bidirectional dual active bridge converter," *IEEE Trans. Power Electron.*, vol. 32, no. 10, pp. 8035–8053, Oct. 2017.

[20] H. Wen and W. Xiao, "Bidirectional dual-active-bridge DC-DC converter with triple-phase-shift control," in *Proc. Appl. Power Electron. Conf. Expo.*, 2013, pp. 1972–1978.

[21] K. Wu, C. W. de Silva, and W. G. Dunford, "Stability analysis of isolated bidirectional dual active full-bridge DC–DC converter with triple phase-shift control," *IEEE Trans. Power Electron.*, vol. 27, no. 4, pp. 2007–2017, Apr. 2012.

[22] J. Huang, Y. Wang, Z. Li, and W. Lei, "Unified triple-phase-shift control to minimize current stress and achieve full soft-switching of isolated bidirectional DC–DC converter," *IEEE Trans. Ind. Electron.*, vol. 63, no. 7, pp. 4169–4179, Jul. 2016.

[23] G. Ortiz, H. Uemura, D. Bortis, J. W. Kolar, and O. Apeldoorn, "Modeling of soft-switching losses of IGBTs in high-power high-efficiency dual-active-bridge DC/DC converters," *IEEE Trans. Electron Devices*, vol. 60, no. 2, pp. 587–597, Feb. 2013.

[24] T. Hirose, M. Takasaki, and Y. Ishizuka, "A power efficiency improvement technique for a bidirectional dual active bridge DC–DC converter at light load," *IEEE Trans. Ind. Appl.*, vol. 50, no. 6, pp. 4047–4055, Nov./Dec. 2014.

[25] H. Shi, H. Wen, J. Chen, Y. Hu, L. Jiang, and G. Chen, "Minimum-reactive-power scheme of dual active bridge DC-DC converter with 3-level modulated phase-shift control," *IEEE Trans. Ind. Appl.*, vol. 53, no. 6, pp. 5573–5586, Nov./Dec. 2017.

[26] B. Zhao, Q. Song, W. Liu, and W. Sun, "Current-stress-optimized switching strategy of isolated bidirectional DC-DC converter with dual-phase-shift control," *IEEE Trans. Ind. Electron.*, vol. 60, no. 10, pp. 4458–4467, Oct. 2013.

[27] B. Feng, Y. Wang, and J. Man, "A novel dual-phase-shift control strategy for dual-active-bridge DC-DC converter," in *Proc. Annu. Conf. IEEE Ind. Electron. Soc.*, 2014, pp. 4140–4145.

[28] N. Hou, W. Song, and W. M, "Minimum-current-stress scheme of dual active bridge DC-DC converter with unified-phase-shift control," *IEEE Trans. Power Electron.*, vol. 31, no. 12, pp. 8552–8561, Dec. 2016.

[29] B. Zhao, Q. Song, and W. Liu, "Efficiency characterization and optimization of isolated bidirectional DC-DC converter based on dual-phase-shift control for DC distribution application," *IEEE Trans. Power Electron.*, vol. 28, no. 4, pp. 1711–1727, Apr. 2013.

[30] B. Zhao, Q. Song, W. Liu, and Y. Sun, "A synthetic discrete design methodology of high-frequency isolated bidirectional DC/DC converter for grid-connected battery energy storage system using advanced components," *IEEE Trans. Ind. Electron.*, vol. 61, no. 10, pp. 5402–5410, Oct. 2014.

[31] F. Krismer and J. W. Kolar, "Efficiency-optimized high-current dual active bridge converter for automotive applications," *IEEE Trans. Ind. Electron.*, vol. 59, no. 7, pp. 2745–2760, Jul. 2012.

[32] B. Zhao, Q. Song, W. Liu, G. Liu, and Y. Zhao, "Universal high-frequency-link characterization and practical fundamental-optimal strategy for dual-active-bridge DC-DC converter under PWM plus phase-shift control," *IEEE Trans. Power Electron.*, vol. 30, no. 12, pp. 6488–6494, Dec. 2015.

[33] Z. Du, L. M. Tolbert, J. N. Chiasson, and B. Ozpineci, "Reduced switching-frequency active harmonic elimination for multilevel converters," *IEEE Trans. Ind. Electron.*, vol. 55, no. 4, pp. 1761–1770, Apr. 2008.

[34] J. N. Chiasson, L. M. Tolbert, K. J. McKenzie, and Z. Du, "A unified approach to solving the harmonic elimination equations in multilevel converters," *IEEE Trans. Power Electron.*, vol. 19, no. 2, pp. 478–490, Mar. 2004.

[35] L. Meng, T. Dragicevic, J. C. Vasquez, and J. M. Guerrero, "Tertiary and secondary control levels for efficiency optimization and system damping in droop controlled DC–DC converters," *IEEE Trans. Smart Grid*, vol. 6, no. 6, pp. 2615–2626, Nov. 2015.

[36] S. Singh and B. Singh, “Optimized passive filter design using modified particle swarm optimization algorithm for a 12-pulse converter-fed LCI–synchronous motor drive,” *IEEE Trans. Ind. Appl.*, vol. 50, no. 4, pp. 2681–2689, Jul./Aug. 2014.

[37] K. Shen *et al.*, “Elimination of harmonics in a modular multilevel converter using particle swarm optimization-based staircase modulation strategy,” *IEEE Trans. Ind. Electron.*, vol. 61, no. 10, pp. 5311–5322, Oct. 2014.

[38] A. F. Zobaa and A. Lecci, “Particle swarm optimisation of resonant controller parameters for power converters,” *IET Power Electron.*, vol. 4, no. 2, pp. 235–241, Feb. 2011.

Haochen Shi was born in Hubei, China, in 1992. He received the B.S. degree from Three Gorge University, Yichang, China, in 2014, and the M.Eng. degree from University of Leicester, Leicester, U.K., in 2015, both in sustainable energy technology. He is currently working toward the Ph.D. degree in sustainable energy technology with the University of Liverpool, Liverpool, U.K.

His current research interests include bidirectional dc–dc converter, electrical vehicles, and renewable power conversion system.

Huiqing Wen (M’13) received the B.S. and M.S. degrees in electrical engineering from Zhejiang University, Hangzhou, China, in 2002 and 2006, respectively, and the Ph.D. degree in electrical engineering from the Chinese Academy of Sciences, Beijing, China, in 2009.

From 2009 to 2010, he was an Electrical Engineer working with the Research and Development Center, GE (China) Co., Ltd., Shanghai, China. From 2010 to 2011, he was an Engineer with the China Coal Research Institute, Beijing, China. From 2011 to 2012, he was a Postdoctoral Fellow with the Masdar Institute of Science and Technology, Abu Dhabi, United Arab Emirates. He is presently working as an Associate Professor with the Xi’an Jiaotong-Liverpool University, Suzhou, China. His current research interests include bidirectional dc–dc converters, power electronics in flexible ac transmission applications, electrical vehicles, and high-power, three-level electrical driving systems.

Yihua Hu (M’13–SM’15) received the B.S. degree in electrical motor drives, and the Ph.D. degree in power electronics and drives from China University of Mining and Technology, Jiangsu, China, in 2003 and 2011, respectively.

From 2011 to 2013, he was a Postdoctoral Fellow with the College of Electrical Engineering, Zhejiang University, Hangzhou, China. From November 2012 to February 2013, he was an Academic Visiting Scholar with the School of Electrical and Electronic Engineering, Newcastle University, Newcastle upon Tyne, U.K. From 2013 to 2015, he was a Research Associate with the Power Electronics and Motor Drive Group, University of Strathclyde, Glasgow, U.K. He is presently working as a Lecturer with the Department of Electrical Engineering and Electronics, University of Liverpool, Liverpool, U.K. He has published more than 36 peer-reviewed technical papers in leading journals. His current research interests include PV generation systems, power electronics converters and control, and electrical motor drives.

Lin Jiang (M’00) received the B.S. and M.S. degrees in electrical engineering from Huazhong University of Science and Technology, Wuhan, China, in 1992 and 1996, respectively, and the Ph.D. degree in electrical engineering from the University of Liverpool, Liverpool, U.K., in 2001.

He is presently working as a Reader of electrical engineering with the University of Liverpool. His current research interests include the optimization and control of smart grids, electrical machines, power electronics, and renewable energy.